Geothermics 141 (2026) 103747

Contents lists available at ScienceDirect

Geothermics

journal homepage: www.elsevier.com/locate/geothermics

ELSEVIER

Field to laboratory assessment of subsurface thermal conductivity: A geothermal case study in Slovenia

Karlo Borko [a,*], Fiona M. Chapman [b], Jasmin Raymond [b], Grzegorz Ryżyński [c], Nina Rman [a]

[a] Geological Survey of Slovenia, Dimičeva ulica 14, 1000 Ljubljana, Slovenia
[b] Institut national de la recherche scientifique, Centre Eau Terre Environnement, Québec, 490 Couronne St, Québec City, QC G1K 9A9, Canada
[c] Państwowy Instytut Geologiczny – Państwowy Instytut Badawczy, ul. Rakowiecka 4, 00–975 Warszawa, Poland

ARTICLE INFO

Keywords:
Distributed temperature sensing
Thermal response test
Groundwater flow
Thermal conductivity
Krško Basin

Abbreviations: BHE, Borehole heat exchanger
DTRT, Distributed thermal response test
DTS, Distributed temperature sensing
EOP, Overburden pressure
ETRT, Enhanced thermal response test
FO, Fibre optic
GeoZS, Geological Survey of Slovenia
GSHP, Ground source heat pump
ILS, Infinite Line Source
TCS, Thermal conductivity scanner
TRT, Thermal response test
UTES, Underground thermal energy storage

ABSTRACT

Reliable characterization of subsurface thermal properties is essential for designing efficient shallow geothermal systems and assessing the potential of Ground Source Heat Pump and Underground Thermal Energy Storage systems. The objective of this study is to evaluate the reliability of thermal conductivity estimations from different approaches by comparing three *in situ* methods - conventional Thermal Response Test (TRT), Enhanced Thermal Response Test (ETRT), and Distributed Thermal Response Test (DTRT) - against each other and laboratory measurements on core samples. The tests were conducted in a 100 m deep borehole heat exchanger in the Krško Basin, Slovenia. Laboratory measurements employed needle probes and an optical Thermal Conductivity Scanner (TCS), while *in situ* testing utilized fibre-optic Distributed Temperature Sensing (DTS) for high-resolution temperature profiling. Results show that needle probe measurements consistently underestimate thermal conductivity relative to TCS- and DTS-based methods, by 22% to 48%, mainly due to sample desaturation and limited probe contact. DTS-based ETRT revealed vertical variations and groundwater-flow-influenced zones. Cemented fibre-optic cables introduced greater uncertainty and yielded 44% higher conductivities than the ETRT with the composite cable. TCS yielded thermal conductivities most consistent with *in situ* measurements while providing a favourable balance of time, cost, and reliability of results.

List of symbols and physical quantities

α	Thermal diffusivity (m^2s^{-1})
C	Volumetric heat capacity ($Jm^{-3}K^{-1}$)
c_p	Specific heat capacity ($Jkg^{-1}K^{-1}$)
ΔT	Temperature change (°C)
H	Depth of borehole (m)
k	slope of fluid temperature over the logarithm of time
λ	Thermal conductivity ($Wm^{-1}K^{-1}$)
λ_{eff}	Effective thermal conductivity ($Wm^{-1}K^{-1}$)
m	intercept of fluid temperature over the logarithm of time
n	Number of measurements
Q	Total power input (kW)
R_b	Borehole thermal resistance (mKW^{-1})
SD	Standard deviation
$T_f(t)$	Average fluid temperature (°C)

1. Introduction

Thermal subsurface properties, particularly thermal conductivity (λ) and thermal diffusivity (α), play a critical role in the design, optimization, and performance of shallow and deep geothermal systems. In shallow applications, accurate knowledge of these parameters is crucial for proper sizing of ground-source heat pump (GSHP) and underground thermal energy storage (UTES) systems (Raymond, 2018). At greater depths, information on thermal conductivity contributes to terrestrial heat flux assessments, thereby reducing uncertainty in geothermal exploration (Chapman et al., 2025). These properties also support the interpretation of geophysical data and the refinement of geothermal models (García-Noval et al., 2024; Pambou et al., 2022; Arias-Peñas

* Corresponding author.
E-mail address: karlo.borko@geo-zs.si (K. Borko).

https://doi.org/10.1016/j.geothermics.2026.103747
Received 25 November 2025; Received in revised form 26 May 2026; Accepted 15 June 2026
Available online 20 June 2026

et al., 2015). Thermal properties can be evaluated based on surface samples, core samples, or by *in situ* tests, such as thermal response tests (TRT).

Surface samples are easily collected and offer a cost-effective method to determine thermal properties either in the field, with a needle-probe, or in a laboratory with a needle probe, a transient scanner or steady-state instruments. However, surface sediment samples difficultly picture the effect of substrate variation, *in situ* water saturation and compaction (Woodside and Messmer, 1961). Sediment and bedrock cores provide real-depth samples but increase drilling costs. Core samples better represent subsurface heterogeneity than surface samples, but thermal properties measured do not consider fracturation or scale effect (Li et al., 2024; Albers et al., 2025; Rajver and Adrinek, 2023; Rajaobelison et al., 2025).

An alternative is *in situ* methods applied directly in boreholes (Chapman et al., 2025) or geoprobes (Ma et al., 2022; Hakala and Leppäharju, 2014), such as thermal response tests (TRT). Conventional TRTs are performed in borehole heat exchangers (BHE). A constant heat load is injected into the U-tube and the temperature response of the circulating fluid is monitored at the outflow (Gehlin, 2002; Mogensen, 1983). The infinite line source (ILS) equation is typically used to analyse the thermal response and determine the effective thermal conductivity (λ_{eff}). The ILS equation assumes conductive heat transfer and the singular thermal response results provide an average value of the effective ground thermal conductivity along a given borehole (Ingersoll et al., 1954). However, subsurface heterogeneity and the influence of groundwater flow can difficultly be identified in a convention TRT.

The conventional TRT was expanded by using fibre-optic (FO) distributed temperature sensing (DTS) to record temperature at multiple depths along the borehole (Hakala and Leppäharju, 2014; Acuña et al., 2011; Acuña and Palm, 2013; Fujii et al., 2006). The FO cable was initial installed within the U-tube (Ma et al., 2022) or can be cemented in the borehole. This adaptation of the conventional TRT is known as distributed TRT (DTRT) and can allow to identify heterogeneity but the results remain muted due to the fluid circulation.

Enhanced thermal response tests (ETRT) maintain the same principles, but heat is injected equally along the length of the borehole using heating cables rather than by fluid circulation. This allows for a more controlled and localised thermal input (Albers et al., 2024; Vélez Márquez et al., 2018). In ETRTs, a composite cable (FO-copper) is typically placed in either one side of the BHE U-loop (Radioti et al., 2013) or is suspended in an open well (Liu et al., 2023; De Sousa Figueira et al., 2024). The ILS equation is typically used to analyse the DTS results from both DTRT and ETRT. Although the ILS assumes conductive heat transfer, the high-spatial resolution thermal conductivity profiles resultant from distributed temperature data describes stratigraphic heterogeneity and can allow for conductive and advective heat transfer to be identified in zones with effective thermal conductivity values (Gérard et al., 2021; Nguyen et al., 2026).

The resolution and accuracy of field and lab methods are variable. For example, needle-probe measurements are reported to underestimate λ due to poor thermal contact between the probe and the sample and differences in sample humidity. In contrast, a thermal conductivity scanner typically yields more stable values, thereby providing a better representation of rock material properties. According to Zhang et al. (2018), laboratory methods typically yield λ values that are 35.6% lower than *in situ* measurements because they cannot replicate advection, heterogeneous layers, and the real underground thermal regime. This difference is confirmed by Zhang et al. (2020), who found that ETRT and DTRT values were higher than those of the core samples (measured with Hot Disk TPS 2500S).

Previous studies consistently showed that ETRTs and DTRTs result in effective thermal conductivities (λ_{eff}) that are similar to those obtained from conventional TRT (Mohammadzadeh Bina et al., 2025; Aydin et al., 2024). For example, De Sousa Figueira et al. (2024) reported that thermal conductivity from ETRT was 8% higher than from conventional TRT in gravel and silty sand. In contrast, Vélez Márquez et al. (2018) found the two methods yielded the same λ_{eff} of 1.47 ± 0.03 $Wm^{-1}K^{-1}$ in limestones (Orléans, France), but the ETRT yielded a 15.45% higher average in clay and shale (Québec, Canada). Vieira et al. (2017) likewise observed only minor deviations (4.25% on average) between ETRT and conventional TRT in alternating layers of sand, sandy clay, clayey sand, and weathered rock with groundwater flow.

These findings align with the comprehensive review of advanced TRT techniques by Wilke et al. (2020), who demonstrated that differences between enhanced and conventional TRT are typically below 10%, confirming the reliability of ETRT and DTRT as suitable alternatives for determining effective thermal conductivity and highlighting their capability to detect lithological changes and groundwater-affected intervals that conventional TRT cannot resolve.

The objective of this research is to evaluate the difference in thermal conductivity values obtained from core samples or *in situ* within a given borehole by four needle probe sensors, a thermal conductivity scanner, conventional TRT, DTRT, and ETRT. Notably, this includes results from ETRT with a cemented FO cable and ETRT with suspended FO cable. The impact of cable position was not addressed in previous research. Globally, we aimed to expand knowledge on the uncertainty of each method applied to a grained clastic sediment environment. We anticipate the difference between methods to be between 5 and 10%. This study also represents the first application of DTS in Slovenia for geothermal research, having previously being used only for dam monitoring (Humar et al., 2022).

2. Study site

2.1. Geological setting

The study site is located on a flat agricultural terrain near the Krka River at 152 m a.s.l in Brod v Podbočju. It is in southeastern Slovenia on a Neogene-age structural syncline that marks the southwestern margin of the Krško Basin (Fig. 1c) (Ivančič et al., 2025). The uppermost geological units consist of Quaternary calcareous and siliciclastic gravels and sands. Beneath these, Pliocene sediments are predominantly clay and sandy clay, with occasional gravel clasts and pebbles. These layers overlie Upper Miocene deposits, which are fine-grained and poorly lithified with low degrees of cementation and compaction, up to 1850 m thick (Poljak, 2017).

Coring was performed in the Upper Miocene Drnovo Formation, widely present in the Krško Basin (Ivančič et al., 2024). It consists primarily of well-to-poorly lithified calcareous (dolomite and calcite) siltstone and marl, locally containing more quartz-sand layers in the upper parts and is up to 300 m thick. These deposits form an aquitard (Mali et al., 2021).

The Mesozoic carbonate basement outcrops approximately 1 km south-east in the Gorjanci Hills (1178 m a.s.l.). Based on Gosar et al. (2005), the depth to basement rocks at the BHE site is estimated between 200 and 400 m.

2.2. Regional geothermal settings

The Krško Basin is one of the key geothermal areas in the western Pannonian Basin (Rman et al., 2020) and lies within a tectonically active zone between the Dinarides and the Pannonian Basin System (Ivančič et al., 2025). The thick covering of low-permeable sediments serves as a thermal blanket, enabling formation of the regional Čatež geothermal aquifer in fractured and faulted Mesozoic carbonate rocks (Lapanje, 2006). Geothermal gradients in the basin vary due to the influence of heat conduction through sedimentary layers and convective flow in fissured basement. Geophysical surveys and a heat flow density average of 54 mWm^{-2} indicate a convection-driven hydrothermal system without magmatic influence (Rajver and Ravnik, 2003). Deep

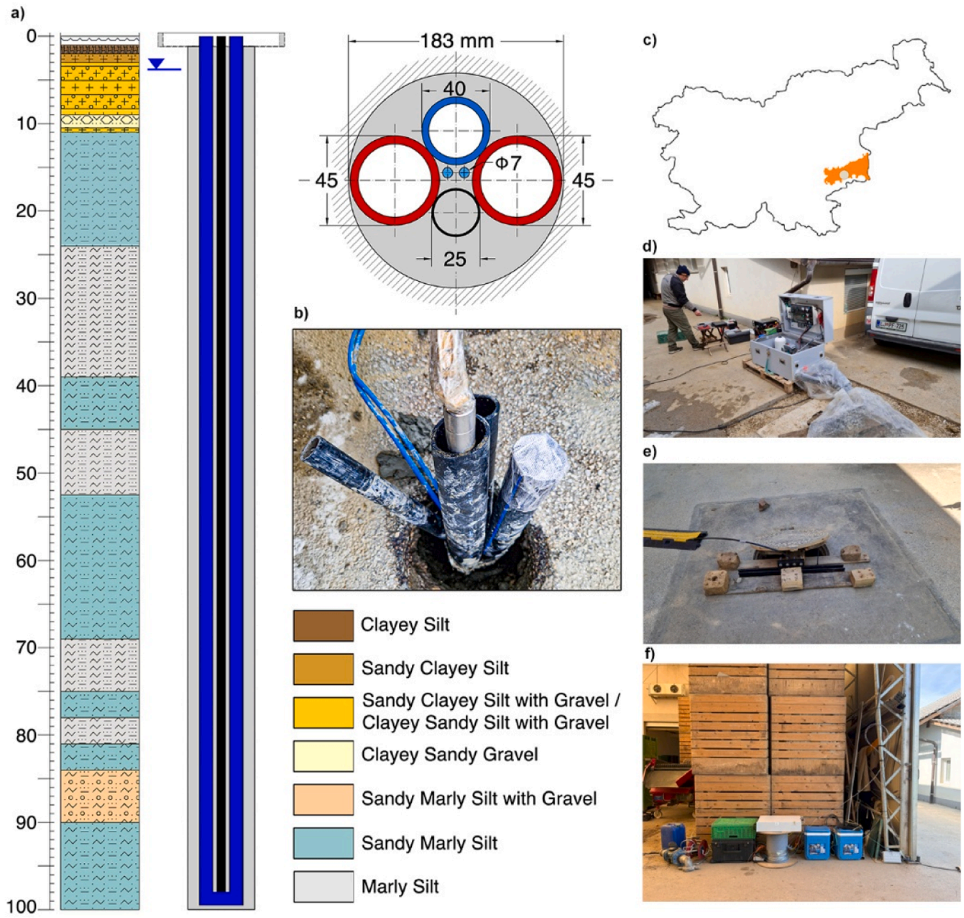

Fig. 1. a) Geological and technical cross-section of GCF-1/24; b) BHE tubes and FO cables; c) borehole location; d) DTRT setup; e) and f) ETRT setup.

groundwater (up to 3 km) rises along the faults to create thermal springs at up to 64 °C (Rajver and Ravnik, 2003; Rupf et al., 2020; Verbovšek, 1988).

A second, slightly less pronounced geothermal anomaly is located near the villages of Malence and Kostanjevica na Krki (Rajver and Ravnik, 2003). Approximately 1.5 km west of the study site, an 800 m deep borehole, SI-1/86, was drilled through Neogene clayey silt and reaches Triassic dolomite at 630 m. The geothermal gradient for Neogene sediments is 41.9 °C km^{-1} and the average thermal conductivity of 6 cores from 101 to 592 m depth was 1.67 W m^{-1}K^{-1}. Silty marls down to 406 m have an average λ of 1.49 W m^{-1}K^{-1} (Rajver and Adrinek, 2023). The heat flow density is estimated at 69 ± 3 mW m^{-2} without a paleoclimatic correction (Rajver and Ravnik, 2003).

There are two 100 m deep boreholes located approximately 2 km west of the study site: V-8/86 in Malence, and V-7/85 in Kostanjevica na Krki near Topličnik thermal spring. Borehole V-8/86 is located primarily in Neogene clayey silt has a geothermal gradient of 54.2 °C km^{-1}. It is used for ground-air temperature monitoring (Dědeček et al., 2013). Borehole V-7/85 penetrates marl and clayey marl and has a geothermal gradient of 95.2 °C km^{-1}. Paleoclimate corrections were applied to both profiles based on Haenel et al. (1988). An additional two boreholes TG-1/12 (101 m) and PDt-1/03 (848 m) located 400 m north, and 700 m east of the study site are located in clayey silts. The geothermal gradients are 15.9 °C km^{-1} (from surface to 100 m) and 13.9 °C km^{-1} (from surface to 396 m), respectively.

2.3. Research borehole - BHE

2.3.1. Technical design

The investigated BHE is a100-meter-deep research borehole labelled GCF-1/24. A single U-tube from MuoviTech is installed (outer diameter 45 mm, turbocollector PE100, $\lambda = 0.4$ W m^{-1}K^{-1}, $c_p = 1.9$ Jkg^{-1}K^{-1}) with no weight attached at the bottom. The tremie pipe (outer diameter 25 mm) was used for cementing and was not removed nor tube separators were used as this is the usual drilling practice in Slovenia. The borehole was cemented with Portland cement UNIVERSAL from Salonit Anhovo. The monitoring tube (outer diameter 40 mm, trapipes PE100, $\lambda = 0.38$ W m^{-1}K^{-1}) was closed at the bottom, and both, the U-tube and the monitoring tube, are filled with tap water. Prior to installation, tubes were bound together at 5 m intervals with plastic foil, protecting the FO cables in the middle (Fig. 1b).

This is the first borehole in Slovenia that is installed with a cemented FO cable, grouted between four pipes (Fig. 1a and 1b). The cable is B1011A ACOLAN CLT STD ZH loose-fit tube with 4 multimode optic fibres, 50/125 µm, OM3. Its nominal diameter is 7 mm (ACOME, n.d.). It was installed with a total length of 200 m (100 m each way) and is bent at the bottom without any additional elements.

2.3.2. Lithostratigraphy

The BHE penetrates Quaternary alluvial sediments to ~11 m with a moderately permeable layer of clayey-sandy gravel from 9.0 to 10.5 m. Below, the Drnovo Formation consists of alternating layers of sandy marly silt, marly silt, sandy marl loam, and some pebbles (Fig. 1a). A natural gamma ray log (Fig. 4b) was recorded using a Robertson Geologging TCDS (Temperature/Conductivity/Depth/Single Point resistance) probe. The log signal distinguishes between the Quaternary and the deep Miocene sediments but is otherwise homogeneous. The boundary is at approximately 11 m depth (Fig. 4b). The Miocene sediments extend to the base of the borehole alternating primarily between sandy marly silt and marly silt (Section 2.1.).

2.3.3. Hydrogeology

After drilling, the groundwater level was recorded at 3.77 m below the surface (20,24-11-08). Two core samples (24.0 to 26.0 m and 50.0 to 52.5 m) were recovered and analysed for moisture content, porosity, permeability, grain size distribution and thermal properties. Soil moisture content of both cores was measured immediately after the core extraction (on 20,24-11-06 and 2024–11–07) using the TEROS-10 probe (GeoZS). The average soil moisture for samples at 25.1–25.8 m and 50.0–51.83 m was 34.4% and 30.3%, respectively. These values were considered when interpreting KD2 Pro measurements.

Grain size, porosity, and permeability were measured on two core sections 25.10 to 25.22 m and 50.00 to 50.19 m in the INA Industrija nafte d.d. laboratory (Zagreb). Both samples consist of very fine silt based on grain size distribution and have a clay content of 41.3 wt% and 71.5 wt%, respectively. However, the natural gamma activity is below 30 API in each core segment which implies a low clay content (Fig. 4b). Investigated silts may contain non-radioactive clay minerals (*e.g.*, kaolinite) with the presence of calcareous or siliceous components. Porosity and permeability were measured on core samples with an overburden pressure of 15 and 20 bar. The 25.10 to 25.22 m core decreased in porosity from 35.0% to 34.1% and in intrinsic permeability from 44.28 to 24.02 mD. The porosity and permeability of the 50.00 to 50.19 m core decreased from 37.3 to 35.3% and from 1570.51 to 497.25 mD, respectively.

2.3.4. Temperature with depth distribution

The average annual air temperature (1991 to 2020) was 10.9 °C at the airport Cerklje ob Krki (10 km NE of the study site) (ARSO, 2025).

An initial temperature-depth (T–z) profile was measured in the borehole using the Robertson Geologging well-log equipment, having a spatial resolution of 1.0 cm and a temperature accuracy of 0.001 °C, one hour after drilling and before BHE installation (2024–11–08). The borehole was naturally filled with groundwater. After installation, manual temperature profiles were measured using the Hydrotechnik GmbH Level-Temperature meter type 110 (GeoZS) prior to TRTs (2025–02–18, 2025–04–18, 2025–06–03) and after the final ETRT (2025–06–20; Fig. 4a). Values were recorded at 1 m intervals with 15 s stabilization periods at each depth (accuracy: 0.1 °C). After borehole construction, a Star-Oddi centi-TD temperature sensor was installed at the bottom of the monitoring tube and collected hourly data from 2024–11–09 to 2025–06–12 (accuracy of 0.032 °C).

Temperature data in Figs. 2 and 4 are shown below groundwater level (3.77 m below surface). A negative geothermal gradient is present over the first 48 m with seasonal variation from the surface to 9 m (Fig. 4a). Between 9 and 11 m, the profile is influenced by an aquifer, which temporarily stabilizes the temperature. From 11 to 48 m depth, the temperature decreases gradually, indicating a low thermal conductivity. The temperature gradient stabilizes at 5.83 °Ckm^{-1} from 48 to 100 m. According to the centi-TD temperature sensor, the temperature at 100 m remains constant at 12.65 (± 0.03) °C.

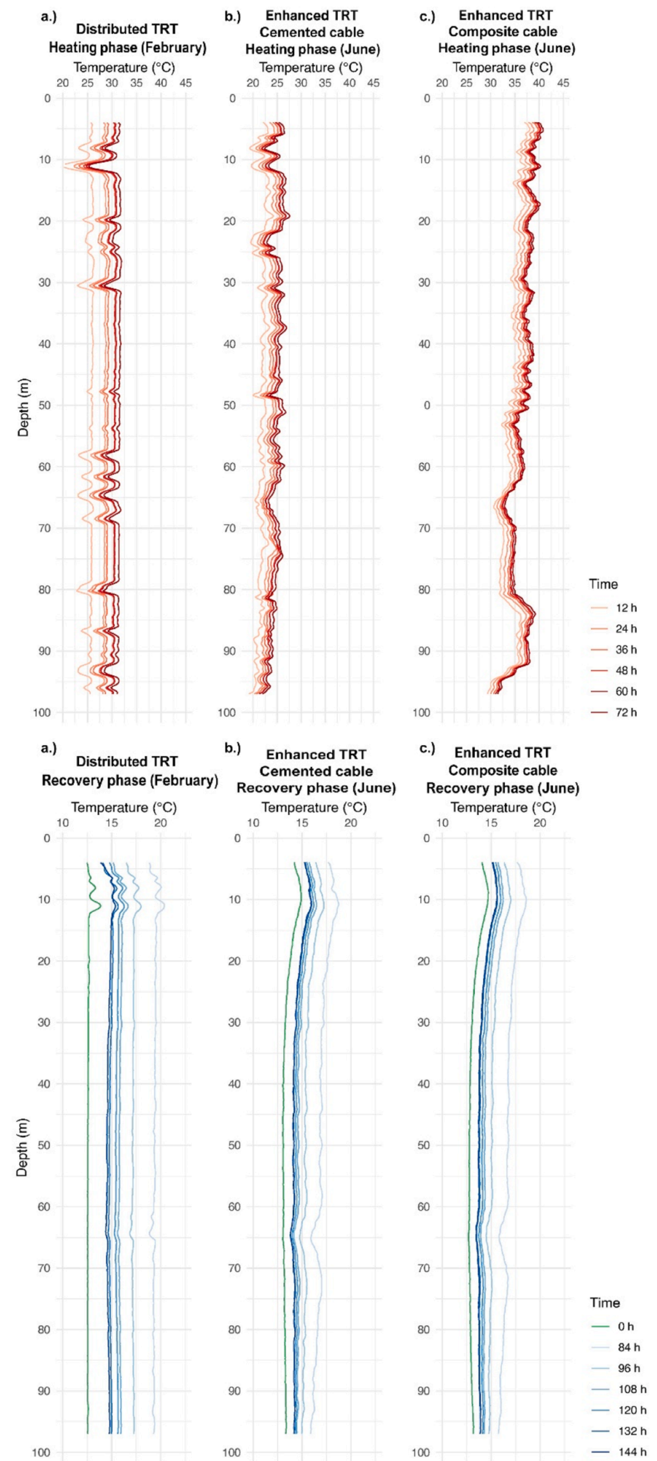

Fig. 2. Temperature-depth (T-z) profiles for 12 h steps of TRTs with heating and recovery phases.

3. Methods

3.1. Thermal conductivity from core samples

3.1.1. KD2 pro probe used in the field

Thermal conductivity was measured using a KD2 Pro needle probe with a total of 16 measurements on 10 core samples. The SH-1 double-needle (Decagon Devices, Inc., 2016) was used to measure thermal conductivity, thermal resistance (ρ), thermal diffusivity (α), and volumetric heat capacity (C) on bulk material. Measurements were performed on fresh core material at depths of 25.10 m, 25.70 m, 50.00 m, 51.05 m, and 51.73 m, with a 2 min measurement time. Thermal conductivity and thermal resistance were also measured at the same core intervals using a TR-1 single-needle probe with a 5-minute measurement time. There was a 15 min pause before the first measurement and between consecutive measurements. Thermal paste was applied to reduce contact resistance. The SH-1 probe was inserted perpendicular to the core axis, whereas the TR-1 probe was inserted along the core axis.

3.1.2. Thermal conductivity scanner used in the laboratory

The TCS operates with samples based on the principle of non-contact optical scanning (Rajver and Adrinek, 2023; Popov et al., 1983). TCS measurements were taken at GeoZS a few days after core extraction (2024–11–11). The samples were painted with black acrylic to maximize absorbance during measurement. λ and α were measured on five segments from the upper core and nine segments from the lower core, ranging from 8 to 22 cm long. The core samples were 11.4 cm wide and raised by ~0.3 cm to reduce the effect of circularity; therefore circularity correction was not applied.

3.1.3. TEMPOS thermal properties analyzer used in the laboratory

Thermal properties were also measured on the core sample from 51.05 to 51.17 m using the TEMPOS Thermal Properties Analyzer (METER Group, Inc., 2018) at the Polish Geological Survey (PGI). The sample was transported in a plastic bag and stored in a refrigerator at PGI prior to the measurements (2025–11–25). Evaluation of λ, α, and C was performed using the SH-3 dual-needle probe, while λ and ρ were determined using the TR-3 single-needle probe. The SH-3 probe was inserted perpendicular to the core axis, while the TR-3 probe was inserted along the core axis. Heat was applied for 30 s with the SH-3 probe and for 5 min with the TR-3 probe, followed by 1.5- and 5 min recovery periods, respectively. There was a 15 min pause before the first measurement and between consecutive measurements. Thermal paste was applied between the probe and the sample surface.

3.2. Experimental setup for conventional, distributed and enhanced thermal response tests (TRT)

No disturbances or technical interventions were carried out on either the U-tube or the monitoring tube during the heating or recovery phases of any TRTs. All components remained in place and undisturbed throughout testing.

3.2.1. Conventional TRT and DTRT

A TRT device (Adrinek and Janža, 2025) was used for the conventional TRT. It was connected to the U-tube on 2025–02–18. First, the undisturbed temperature was measured with a T-z profile (Section 3.3.). The system was then pre-heated for 1 h to stabilize the system, purge trapped air and measure the average starting temperature at the wellhead.

The BHE was heated for 77.3 h at 5.57 kW (55.7 W m^{-1}) with an average water flow rate of 0.48 l s^{-1}. Temperature changes were monitored using both the conventional TRT PT-1000 temperature probe (accuracy ±0.5 °C) for wellhead output and input (every minute) and the cemented FO cable (every 10 min; Fig. 2). Thermal recovery was then monitored without water circulation for 65 h.

During the conventional TRT, temperature was measured along the cemented FO cable. This resulted in a DTRT with temperature measurements during heating and recovery.

3.2.2. Enhanced TRT

An undisturbed temperature profile was measured as described in Section 3.3.

The ETRT was performed from 2025–06–05 to 2025–06–12, using both the cemented FO cable (Section 2.3) and the temporarily installed composite heating-FO cable. It is a loose-tube, LWL-outdoor hybrid A-DSQ(ZN)B2Y 1 × 4G50/125 + CU 4 × 0.5 mm^2 for outdoor use. It consists of 4 multimode fibres and 4 copper wires, with an 11 mm diameter. The copper wires have a 1.75 mm diameter and a resistance of 36.6 Ω km^{-1} (at 20 °C) (Voges, L.W., 2011). The copper cables were connected in two parallel circuits. It was installed as freely hanging in one of the U-tubes.

The Silixa XT-DTS M interrogator (Silixa Ltd., 2022) was used to record FO temperatures. It operates on the principle of Raman-based backscattering in multimode optical fibres; the Stokes-to-anti-Stokes wavelength ratio is temperature-dependent (Kłonowski et al., 2024), supporting sensing ranges of up to 10 km. Three optical channels were used. Data was sampled at 25 cm with an accuracy of 0.01 °C and spatial resolution of ~65 cm. The data was recorded every 2 min. A double-ended configuration was used for the composite cable, and a single-ended configuration was used for the cemented cable.

Dual PT-100 reference temperature probes were put in warm (~30 °C) and cold calibration baths (~0 °C). The warm bath was maintained by an aquarium heater and ice, or ice packs, were added to the cold bath daily. A bubbler was placed in each calibration bath to avoid stratification.

The power supply heater (EA-PS 9040–170 3 U) (EA Elektro-Automatik KG., n.d.) was used at an output of 140 V DC and 17.7 A with a maximum output power of 2620 W. Heat was injected for 77 h through the composite cable at an average heat injection rate of 24.67 W m^{-1}. Temperature was measured during the recovery phase for 89 h.

3.3. Thermal conductivity assessment from TRT

The slope method, which is a simplification of the Infinite Line Source (ILS) equation, was used to interpret the data. The transient ILS equation describes one-dimensional (radial) heat transfer in the ground caused by a heat source of infinite length.

The outcome of TRTs is a curve of the average fluid temperature over time (Tinti et al., 2015). Based on the simplified ILS equation, the average temperature of the heat carrier fluid ($T_f(t)$) increases logarithmically during late heat injection time (t) (VDI-Gesellschaft Energie und Umwelt (GEU), 2020):

$$T_f(t) = k \cdot \ln t + m \tag{1}$$

where m is the intercept of fluid temperature over the logarithm of time (related to the undisturbed ground temperature and borehole resistance), k is the slope of fluid temperature over the logarithm of time, which is inversely proportional to the ground λ.

This slope-based expression originates from the ILS formulation of the temperature change (Vasseur and Demongodin, 1995) (Eq. (2)):

$$\Delta T(t) = \frac{q'}{4\pi\lambda_{eff}} \ln\left(\frac{t}{t_0}\right) \tag{2}$$

where $\Delta T(t)$ is the temperature increment relative to the undisturbed ground temperature, q' is the linear heat input along the borehole (W m^{-1}), λ_{eff} is the effective ground thermal conductivity (W $m^{-1}K^{-1}$), t is the elapsed heating time, and t_0 is a characteristic time constant introduced to avoid the singularity at $t = 0$.

Eq. (2) can be rearranged to estimate the effective thermal conductivity as a function of the slope (k; Eq. (3)):

$$\lambda_{eff} = \frac{Q}{4 \cdot \pi \cdot H \cdot k} \tag{3}$$

where Q is the total power input [kW], and H is the depth [m] of the BHE.

The assumptions of the ILS equation are the following:

- heat is solely transferred radially;
- the ground is homogeneous with uniform thermal properties;
- the thermal properties of the borehole components are not explicitly included in the analysis, which assumes the borehole itself acts as the heat source;
- the ground has a uniform initial temperature before the test and the temperature remains unchanged at infinite radial distance; and
- heat is uniformly injected or extracted along the heat source (Gehlin, 2002; VDI-Gesellschaft Energie und Umwelt (GEU), 2020).

In practice, these assumptions are rarely met. However, ILS has proven useful when:

- conductive heat transfer dominates;

- vertical temperature variation due to geothermal gradient and seasonal surface effects does not significantly influence the estimation of λ and potentially thermal resistance of the borehole (R_b);
- temperature changes caused by drilling and borehole installation have stabilized; and
- both theoretical and physical minimum time criteria are respected (VDI-Gesellschaft Energie und Umwelt (GEU), 2020).

The conventional TRT was interpreted using the ILS model in both the heating and recovery phases, taking into account the superposition principle for the later. The DTRT analysis was based on the recovery data. For DTRT and ETRT, thermal conductivities were calculated from the slope of the recovery data between 113 h and 142 h (Fig. 2) at every point, with 25 cm intervals (Fig. 4c).

Zones of conductive and advective heat transfer were identified based on increased thermal conductivity values in sections where no change in lithology was observed, either in the geological column (Fig. 1a) or with the gamma ray log (Fig. 4b) (Vasseur and Demongodin, 1995).

4. Results

4.1. Thermal conductivity from core samples

Table 1 presents the measured thermal conductivities using dual-needle, single-needle, and TCS on core samples. The dual-needle methods (TEMPOS SH-3 and KD2 Pro SH-1 probes) yielded thermal conductivity values for the exact same measuring interval (51.05–51.17 m) that differ by 0.05 W $m^{-1}K^{-1}$ (3.94%). The single-needle probe measurements (TEMPOS TR-3 and KD2 Pro TR-1 probes) differed by 0.07 W $m^{-1}K^{-1}$ (6.6%). The average λ recorded by the single- and double-probe needle differ by 0.68%.

The mean λ measured by the TCS was 1.72 W $m^{-1}K^{-1}$ (± 0.10 W $m^{-1}K^{-1}$). The λ of deeper cores (±0.10 W $m^{-1}K^{-1}$) is more variable than shallow cores (± 0.02 W $m^{-1}K^{-1}$). On average, the λ of deeper cores (50.00 to 52.55 m) are 8.45% higher than shallow cores (24.13 to 25.8 m).

4.2. Temperature response during conventional and enhanced TRT

The temperature response along the borehole during the heating and recovery phases were variable (Fig. 2). For example, the temperature increased slower and recovered faster than average between 60 and 70 m (Figs. 2 and 3). However, the results were not consistent between the cemented and suspended composite FO cables.

The cemented FO cable recorded 52% lower increase in temperature than the FO of the composite cable during ETRT (Fig. 3b, c). The fastest temperature increase was observed in the composite FO cable within the first 15 min. Afterwards, the temperature increase was governed by the thermal properties of the water in the U-tube and later by heat transfer in the surrounding sediments.

The heat injection rate was higher during the DTRT (55.7 Wm^{-1}) than during the ETRT. However, the DTRT measurements showed an average increase of 18.18 °C across the entire profile by the end of the heating phase, which is 23% lower than that measured on the composite cable during the ETRT. The largest relative increase from T_0 and the highest absolute temperature (40.84 °C) were observed at the ETRT composite cable as the FO cable is in direct contact with the heat source (copper cable).

4.3. Comparison of thermal conductivities from TRTs

The average λ based on the heating and cooling phases of the conventional TRT were 1.55 W $m^{-1}K^{-1}$ and 1.86 W $m^{-1}K^{-1}$, respectively. The λ calculated from the recovery period was 19% higher than that from the heating period. Their joint average was 1.71 W $m^{-1}K^{-1}$. Based on $\lambda(z)$ profiles, five depth segments with different average λ values were identified: 3.77–9 m, 9–11 m, 11–60 m, 60–72 m, 72–97 m (Table 2).

Cemented FO during ETRT yielded thermal conductivity values that were 16 to 55% higher than those obtained by DTRT, with the largest deviation observed in the 72 to 97 m segment and the smallest in the 9 to 11 m segment. ETRT performed with cemented FO also reports consistently higher values than ETRT performed with a composite cable, with the lowest difference occurring in the 72 to 97 m segment (20.11%) and the highest in the 3.77 to 9 m segment (26.45%). The composite cable configuration further showed 29.45% higher values than DTRT in the 72 to 100 m interval, whereas in the 9 to 11 m segment, λ was estimated 7.24% lower than the DTRT.

The lowest average λ across all tests was evaluated by ETRT with the composite cable in the 9 to 11 m segment (1.41 W m^{-1} K^{-1}), while the highest was obtained by ETRT with the cemented FO in the 72 to 97 m interval (2.87 W m^{-1} K^{-1}). The average λ calculated from the ETRT cemented cable (1.85 W $m^{-1}K^{-1}$) was 24% higher than from the composite cable at depths between 11 and 60 m. Overall, the DTRT values show good agreement with those from the ETRT composite cable. However, unlike the ETRT, the DTRT does not increase from 60 m to the base of the borehole.

DTRT and ETRT on composite cable yielded comparable values; ETRT on composite cable was 12.33% higher, whereas ETRT on cemented FO showed significantly higher values than on composite cable (+22.56%) and DTRT (+37.67%). Depending on the section, the means of both ETRT cables differ for 20.11% to 26.45% in favour of the

Table 1
Results of core thermal conductivity for various core sections and methods. λ – thermal conductivity, SD – standard deviation, and n – number of measurements.

Core interval (m)	Dual-needle						Single-needle						TCS		
	Tempos SH-3			KD2 Pro SH-1			Tempos TR-3			KD2 Pro TR-1					
	λ ($Wm^{-1}K^{-1}$)	SD	n	λ ($Wm^{-1}K^{-1}$)	SD	n	λ ($Wm^{-1}K^{-1}$)	SD	n	λ ($Wm^{-1}K^{-1}$)	SD	n	λ ($Wm^{-1}K^{-1}$)	SD	n
24.13 – 24.22													1.63	-	1
24.62 – 24.70													1.65	-	1
25.10 – 25.15				1.29	-	1				1.46	-	1	1.64	-	1
25.35 – 25.44													1.60	-	1
25.70 – 25.80				1.19	-	1				1.16	-	1	1.65	-	1
50.00 – 50.22				1.11	0.003	4				1.20	0.121	4	1.72	-	1
50.31 – 50.40													1.81	-	1
50.69 – 50.77													1.88	-	1
51.05 – 51.17	1.29	0.002	3	1.24	-	1	1.15	0.010	3	1.08	-	1	1.94	-	1
51.22 – 51.33													1.75	-	1
51.73 – 51.83				1.25	-	1				1.38	-	1	1.76	-	1
52.00 – 52.09													1.58	-	1
52.29 – 52.40													1.82	-	1
52.46 – 52.55													1.69	-	1

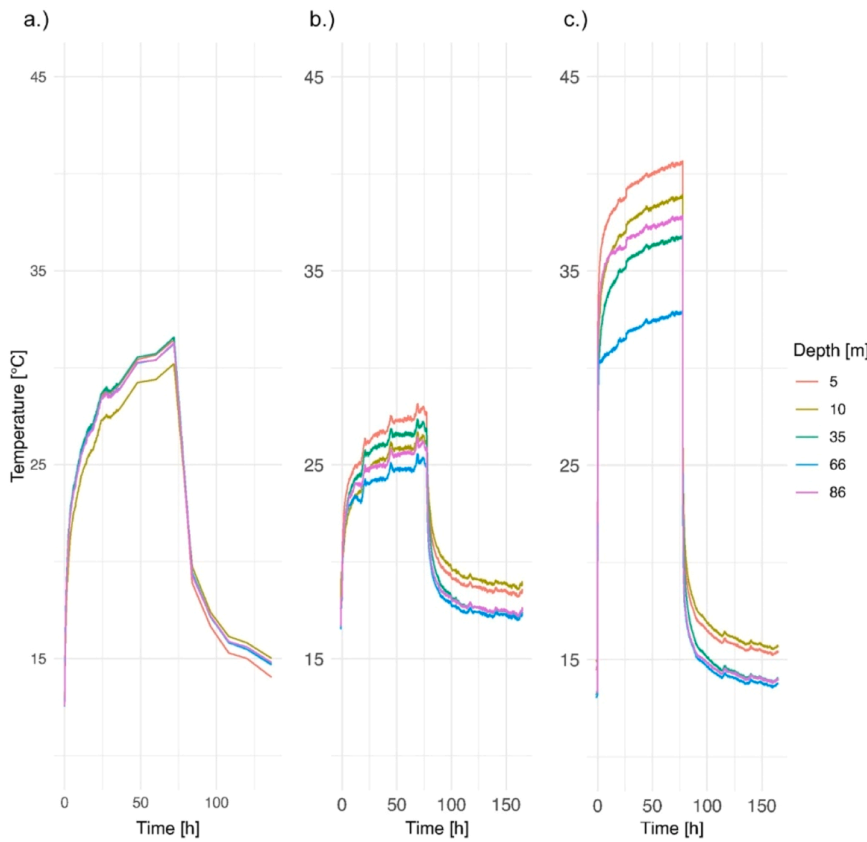

Fig. 3. Temperature–time curves recorded at five selected depths during three test configurations: (a) DTRT with permanently cemented FO cable, (b) ETRT with cemented FO, and (c) ETRT using a composite cable.

Table 2
Thermal conductivity distribution for all three in-situ methods, through five depth ranges, for the total length of the borehole, and segments from which core was recovered.

		DTRT: Cemented Cable			ETRT: Cemented Cable			ETRT: Composite Cable		
BHE segment	Depth (m)	average λ ($Wm^{-1}K^{-1}$)	SD	max λ	average λ ($Wm^{-1}K^{-1}$)	SD	max λ	average λ ($Wm^{-1}K^{-1}$)	SD	max λ
1	3.77–9	1.45	0.04	1.52	1.96	0.04	2.04	1.55	0.03	1.61
2	9–11	1.52	0.03	1.55	1.77	0.03	1.81	1.41	0.04	1.49
3	11–60	1.46	0.05	1.57	1.85	0.07	2.01	1.49	0.04	1.58
4	60–72	1.44	0.02	1.51	2.18	0.27	2.64	1.74	0.16	2.00
5	72–97	1.46	0.01	1.48	2.27	0.28	2.87	1.89	0.22	2.38
Total	3.77–97	1.46	0.04	1.57	2.01	0.27	2.87	1.64	0.22	2.38
Core segments	24–26; 50- 52.5	1.46	0.05	1.52	1.91	0.06	2.00	1.53	0.02	1.55

ETRT cemented FO.

An increase in thermal conductivity was observed from 60 to 72 m, raising the absolute values for both ETRT on the composite cable (34.22%) and on the cemented cable (42.70%), but the λ on the latter remains higher. Deeper, DTRT values remained within a shallower range, while both ETRTs showed a gradual increase in thermal conductivity and the highest averages.

4.4. Comparison of field and laboratory measurements

We compared results from both core sections using 10 methods (Fig. 5). Within the core sections identified, the average λ varies by 13% across the TRT tests (1.71 W $m^{-1}K^{-1}$ ± 0.23 W $m^{-1}K^{-1}$).

The needle probe techniques (*e.g.*, KD2 Pro and TEMPOS) yielded λ values that are 42.14% lower than those from the TCS and TRT methods. The mean λ of needle probe techniques, TCS, and all TRTs were 1.23 ± 0.11 W $m^{-1}K^{-1}$(N = 18), 1.72 ± 0.10 W $m^{-1}K^{-1}$ (N = 14) and 1.68 ± 0.17 W $m^{-1}K^{-1}$ (N = 18), respectively. For the KD2 TR-1 and TCS measurements, values range from 1.08 to 1.46 W $m^{-1}K^{-1}$ and 1.58 to 1.94 W $m^{-1}K^{-1}$, respectively. The minimum unique λ is 1.08 W $m^{-1}K^{-1}$ recorded with the KD2-TR1, and the maximum λ recorded is 1.99 W $m^{-1}K^{-1}$ during ETRT (permanently cemented fibre).

5. Discussion

We hypothesised that thermal conductivities, determined by ten different methods, on two core sections would differ by no >5 to 10%. The thermal conductivity profile of the investigated BHE was expected to be uniform, and silts should exhibit no or minimal groundwater flow. In practice, the applied methodologies presented varied results.

Needle-probes (KD2 Pro, TEMPOS) consistently yielded lower thermal conductivities than TCS and conventional TRT. In relation to TCS, needle-probe results were 7.96 to 44.59% lower (33.92% on average). When compared with the *in situ* TRT methods, the differences remained

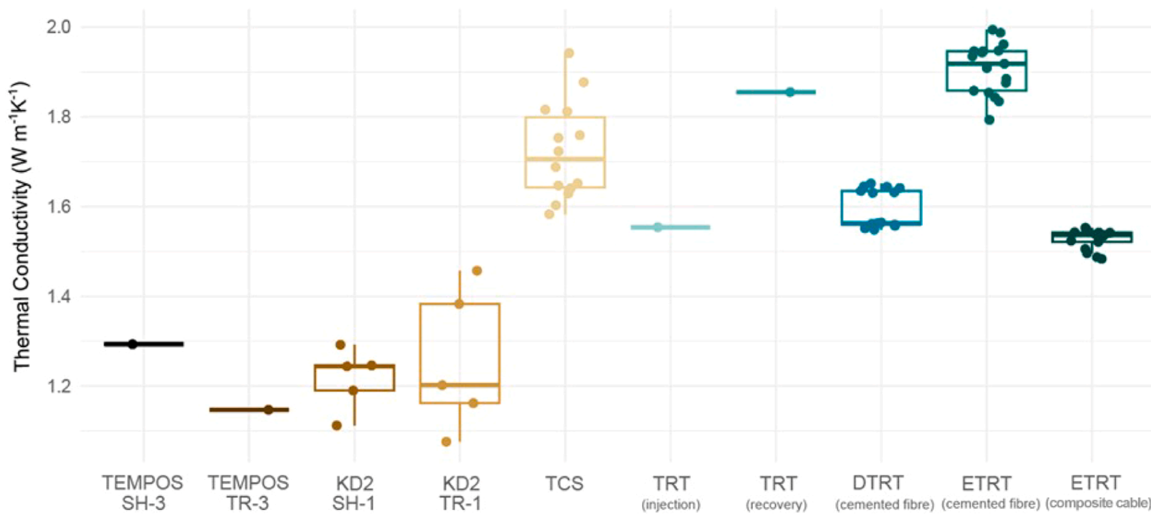

Fig. 5. The box plots represent the distribution of thermal conductivities for different methods, specifically for the core segments. The measurements on core samples are in brown, and in-situ TRT measurements are in blue. Each box represents the interquartile range (IQR; 25th to 75th percentiles).

substantial: needle-probe values are for core segments 22.00% lower than DTRT, 25.57% lower than ETRT with the composite cable, and 40.38% lower than ETRT with the cemented cable. The needle-probe method likely suffered from imperfect thermal contact between the probe tip and the sample surface due to shifting of the natural grain arrangement when inserting the probe (Dalla Santa et al., 2020). The core samples consisted of fine silt; therefore surface roughness is not expected to influence results. Measurements were taken immediately after core extraction therefore desaturation is not expected to be responsible for this difference.

In contrast, the TCS scans a larger bulk volume and is a contactless method of analysis. The TCS measurements yielded the highest absolute λ on the core samples (Table 1). TCS values align more closely with conventional TRT and remain within its standard deviation, which is typically under 10% (Spitler and Gehlin, 2015), despite being obtained under laboratory conditions.

In this study, the DTRT analysis assumed a continuous and constant (uniform) heat injection rate throughout the entire depth. Applying this assumption can result in a smooth thermal conductivity profile as local variations in heat injection rate are not resolved. Heat injection rate in a BHE is expected to decrease with depth (Marcotte and Pasquier, 2008). This can explain the apparent nearly homogeneous thermal conductivity profile along the entire 100 m BHE (Fig. 4c). The maximum-to-minimum value spread was only about 17.26%, whereas ETRTs showed significantly larger fluctuations with 72.58% for the composite cable and 74.42% on the cemented cable.

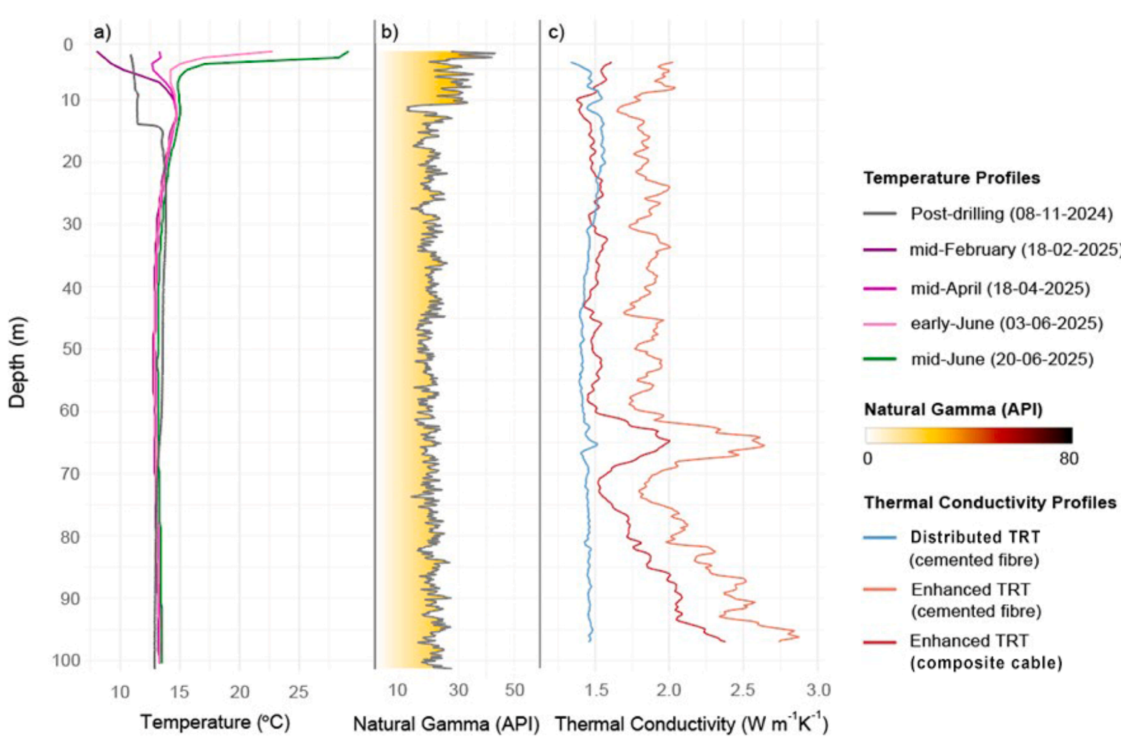

Fig. 4. a) Five temperature-depth profiles measured between 2024 Nov and 2025 June; b) Natural gamma log retrieved in November 2024; c) Thermal conductivity profiles produced from DTRT and ETRT (composite cable and cemented FO).

The ETRT, particularly with the cemented cable, also shows abrupt temperature jumps (Fig. 3b, from 48 to 60 m). Geological reasons are unlikely, given the lithology (Fig. 1a) and the natural gamma log (Fig. 4b). We therefore interpret these anomalies as indications of local heat-transfer irregularities or sensor limitations, most likely caused by installation artifacts or poor thermal contact resulting from inadequate cementing. Such artifacts introduce non-physical temperature discontinuities that distort the true thermal gradient, thereby reducing the reliability of the ETRT profile from the cemented cable and making it difficult to distinguish genuine subsurface thermal features from measurement-related errors (Nguyen et al., 2026).

In the core intervals (Section 4.4), different TRTs showed systematic differences relative to laboratory measurements and among themselves. The ETRT composite cable shows the closest agreement with TCS, being 5.77% lower in the shallow cored interval (24.00 to 26.00 m) and 14.31% lower in the 50 to 52.5 m interval. On average, the λ from ETRT with the composite cable is 11.31% lower than that from TCS results. In comparison, the λ from DTRT is 15.45% lower than that from the TCS. However, the ETRT with the cemented cable yielded, on average, 11.02% higher values than TCS.

For ETRT on both composite cable and cemented FO, the segment with the lowest λ is from 9 to 11 m, while this segment shows the highest λ values for DTRT. As seen from the temperature profiles, which show higher but consistent temperatures, and the natural gamma log, which shows lower density, this segment has higher porosity, is an aquifer of limited thickness, and has limited groundwater flow. Thermal conductivity values for DTRT might be higher because, in February, the aquifer's saturated thickness may have been greater than in June.

ETRT with a cemented cable consistently yielded the highest λ estimates, averaging 22.96% higher than ETRT with the composite cable. Despite this offset, the two ETRT profiles remain strongly correlated in vertical shape (r = 0.96), indicating that the discrepancy is largely a uniform upward shift rather than a structural change in the subsurface response. Over the full profile, the disagreement between the two ETRT configurations corresponds to a moderate RMSE of 0.38 W $m^{-1}K^{-1}$.

The average λ for the length of the borehole from ETRT with a composite cable is 12.33% higher than the DTRT (RMSE: 0.29 W m^{-1} K^{-1}). However, the Pearson correlation coefficient (r = –0.05) indicates that, despite similar values, the two depth-dependent conductivity profiles do not exhibit a meaningful linear relationship. ETRT with the cemented FO deviates most strongly from DTRT, yielding, on average, 37.67% higher values and showing substantially greater scattering (RMSE ≈ 0.61 $Wm^{-1}K^{-1}$).

The depth interval 11 to 60 m was chosen to determine the characteristic λ *for each TRT equipped with the fibre-optic cable.* The mean values were 1.46 W $m^{-1}K^{-1}$ for the DTRT, 1.85 W $m^{-1}K^{-1}$ for the ETRT based on the cemented cable, and 1.49 W $m^{-1}K^{-1}$ for the ETRT based on the coupled cable (Table 2). ETRT composite cable and DTRT are very close to the average value for marly silts in nearby borehole SI-1/86 (mean λ of 1.49 W $m^{-1}K^{-1}$ (Ma et al., 2022)) and all values fall within recorded ranges for fine-grained sediments (~0.5 to 2.5 W $m^{-1}K^{-1}$) (Dalla Santa et al., 2020).

The difference between TRT results is further noted below the compared characteristic segment. For example, there is a sharp increase in λ between 60 and 72 m. DTRT peaks at 65 m is modest ($\lambda \approx 1.52$ W $m^{-1}K^{-1}$), whereas ETRT-cemented peak reaches 2.64 W $m^{-1}K^{-1}$ and ETRT-composite peak 2.00 W $m^{-1}K^{-1}$. This peak is likely due to groundwater flow within the sandy marly silt (Fig. 1a), despite regional geology indicating groundwater flow and no indication in the gamma-ray log (Fig. 4b) (Albers et al., 2024).

In each analysis, the recovery period was examined to ensure that the measured values are representative of the surrounding bedrock. However, the discrepancy between DTRT or ETRT with a composite cable and ETRT with a cemented cable in the characteristic segment suggests that the separation between the direct heat source and the cemented fibre-optic cable may introduce systematic errors. This may also contribute to the difference between peak values between 60 and 72 m, although the notable difference between the DTRT and ETRT-composite cable suggests other contributing factors, such as the variable heat injection rate over the length of the borehole during DTRT.

Below 72 m, an almost linear increase in thermal conductivity was observed for both ETRTs that is not observed with the DTRT assuming a constant heat injection rate with depth. The thermal conductivity increase observed with ETRT if expected true and may be a consequence of multiple factors that influence mineral composition, compaction, permeability, and others. The most likely cause is an increase in the quartz ratio ($\lambda \approx 7.7$ W $m^{-1}K^{-1}$) and a decrease in the calcite ($\lambda \approx 3.6$ W $m^{-1}K^{-1}$) fraction (Horai and Simmons, 1969). This change would not significantly affect the gamma ray log (Fig. 4b). Increased porosity could occur in the sandy clayey silt with gravel, identified between 84–90 m, but we assume only stored, non-flowing water ($\lambda \approx 0.6$ $Wm^{-1}K^{-1}$), which would lead to a gradual increase in thermal conductivity, and not an instant increase as with flowing water. The sediment compaction may also contribute to the λ increase (Beziat et al., 1988).

In the Krško basin, compaction of silt and marl typically begins at approximately 90 m. Compaction decreases porosity as quantified by Beziat et al. (1988), who highlighted an exponential increase in saturated thermal conductivity with decreasing porosity, which would not be observed on a natural gamma ray log (Šumanovac, 2012). As we observe a linear increase in thermal conductivity below 72 m, this could indicate that compaction at our site, at the basin's margin, occurs at significantly shallower depths.

Albers et al. (2024) initially attributed a pronounced increase in λ at the base of an ETRT profile to groundwater advection but later cautioned that splice artefacts or U-bends in FO could generate spurious temperature gradients. We observe this effect in the last three meters of the BHE, where data was discarded. This effect is not expected to extend further along the profile.

An additional source of uncertainty stems from differences in measurement accuracy. Lillo et al. (2022) evidenced that the temperature difference between single- and double-ended configurations of the FO cable can be as high as 2.0–2.2 °C. For the ETRT composite cable, a double-ended configuration was used, enabling back-signal measurement from both ends of the fibre-optic cable. This method significantly reduces the influence of a weak signal and improves loss compensation, thereby increasing the accuracy of the temperature profile. In contrast, a single-ended configuration was used for the ETRT cemented cable, which relies on measurements in only one direction. This approach is more sensitive to variations in optical properties along the cable and signal loss, which can lead to larger deviations in calibration and final results. Therefore, differences between the two measurement types cannot be attributed exclusively to construction characteristics; they also reflect measurement methodology. However, our temperature difference is much higher (Fig. 3), 0.42 °C on average and should be considered further.

Thermal conductivity also varied with the chosen interval time interval to reproduce observations (Beier, 2021); differences between methods might be smaller if we used different time intervals during the recovery period for each technique, rather than a uniform interval across all methods. We used 113 to 142 h as the linearity interval each test, with ln(t) used to quantify the inherent variability between methods under uniform conditions. However, because of the higher heat injection rate for DTRT and the different heater-sensor configuration for the ETRT with cemented cable, it would be reasonable to use adjusted (method-specific) time intervals. The distance between the FO sensor and the heat source, although small (2.25 cm), can cause a time shift in the temperature response, which may affect the slope of the curve and thus the results.

Numerical simulations of each configuration, DTRT, ETRT with cemented cable, and ETRT with composite cable could help confirm whether this offset is responsible for the observed differences and quantify the magnitude of the resulting biases.

6. Conclusion

Ten methods were applied to evaluate thermal conductivity (λ) in the field, the laboratory, and *in situ*, revealing systematic differences among the approaches.

Needle-probe measurements (KD2 Pro, TEMPOS) consistently underestimated λ by 22% to 40% relative to all other methods, confirming their limited reliability and indicating a risk of geothermal system oversizing if used directly.

Laboratory Thermal Conductivity Scanner (TCS) results showed good agreement with *in situ* methods. TCS values were, on average, 18.03% higher than DTRT, 12.63% higher than ETRT with a composite cable, and 9.78% lower than ETRT with a cemented cable, indicating that TCS provides a robust approximation of subsurface thermal conductivity.

Conventional TRT yielded average λ values comparable to TCS, with an overall difference of +1.10%, confirming that conventional TRT is sufficient for homogeneous, fine-grained, low-permeability settings where heat transfer is predominantly conductive.

Among distributed methods, DTRT and ETRT performed with a composite cable showed the closest agreement, with ETRT composite values being 10.98–12.33% higher than DTRT, demonstrating strong consistency between these two approaches.

In contrast, ETRT conducted with a cemented fiber-optic cable produced systematically higher thermal conductivity values, exceeding DTRT by 27.36–37.67% and ETRT composite by 22.56%, indicating significant measurement bias likely related to sensor installation and configuration.

Overall, TCS, conventional TRT, and ETRT using a composite cable produced consistent thermal conductivity estimates within acceptable uncertainty, whereas needle-probe methods and ETRT with a cemented fiber-optic cable showed systematic deviations.

The results demonstrate that method selection and sensor configuration strongly influence thermal conductivity estimates and should be carefully considered in geothermal system design.

Funding sources

Slovenian Research and Innovation Agency.
Ministry of Agriculture, Forestry and Food.
UNESCO International Geoscience Programme (IGCP).
Natural Sciences and Engineering Research Council of Canada.

AI statement

Artificial intelligence (AI) tools were used to support data processing, visualization, and manuscript preparation. Specifically, ChatGPT (OpenAI, June 2024 version) assisted in writing and debugging R code, selecting appropriate methods for graphical interpretation, and refining the text's structure and clarity. All scientific interpretations, methodological decisions, and final edits were made by the authors.

CRediT authorship contribution statement

Karlo Borko: Writing – review & editing, Writing – original draft, Formal analysis, Data curation. **Fiona M. Chapman:** Writing – review & editing, Writing – original draft, Methodology, Formal analysis, Data curation, Conceptualization. **Jasmin Raymond:** Writing – review & editing, Supervision. **Grzegorz Ryżyński:** Writing – review & editing. **Nina Rman:** Writing – review & editing, Writing – original draft, Supervision, Project administration, Methodology, Funding acquisition.

Declaration of competing interest

The authors declare the following financial interests/personal relationships which may be considered as potential competing interests:

Karlo Borko reports financial support was provided by Slovenian Research and Innovation Agency. Fiona M. Chapman reports financial support was provided by UNESCO International Geoscience Programme (IGCP). Karlo Borko reports financial support was provided by Government of the Republic of Slovenia Ministry of Agriculture Forestry and Food. Fiona M. Chapman reports financial support was provided by Natural Sciences and Engineering Research Council of Canada. Nina Rman reports financial support was provided by Slovenian Research and Innovation Agency. Nina Rman reports was provided by Government of the Republic of Slovenia Ministry of Agriculture Forestry and Food. Nina Rman reports financial support was provided by UNESCO International Geoscience Programme (IGCP). Jasmin Raymond reports financial support was provided by UNESCO International Geoscience Programme (IGCP). Fiona M. Chapman reports financial support was provided by Slovenian Research and Innovation Agency. If there are other authors, they declare that they have no known competing financial interests or personal relationships that could have appeared to influence the work reported in this paper.

Acknowledgements

The BHE was drilled within project V1-2213 GeoCOOL FOOD – Cold storage of food using shallow geothermal energy, funded as a Targeted Research Program "Our Food, Rural Areas and Natural Resources" by the Slovenian Research and Innovation Agency (ARIS) and the Ministry of Agriculture, Forestry and Food. Research and writing were supported by ARIS within the Young Researcher Program of K. Borko, research core funding No. P1-0020 Groundwater and Geochemistry, and I0-007 Geological Information Center. Collaboration was facilitated by the UNESCO IGCP project 636 and the Geo-OPT project, co-funded by ARIS under the Developmental Funding Pillar. Participation of F. Chapman in field work was partly funded by the Natural Sciences and Engineering Research Council of Canada.

The authors thank Farm Turk for the permission to drill BHE, Stefan Hoyer from the GeoSphere Austria and Andrej Vidmar from the Faculty of Civil Engineering and Geodesy University of Ljubljana for borrowing the equipment, Jan Udovč and Simon Mozetič for geophysical logging, Dušan Rajver for geothermal datasets, and Kristina Ivančič for the lithological profile.

Data availability

Data and codes are available as supplementary material.

References

ACOME, n.d. ACOLAN Optical – CLT STANDARD ZH: ecatalogue. Technical datasheet.

Acuña, J., Mogensen, P., Palm, B., 2011. Distributed thermal response tests on a multipipe coaxial borehole heat exchanger. HVAC&R Res. 17, 1012–1029. https://doi.org/10.1080/10789669.2011.625304.

Acuña, J., Palm, B., 2013. Distributed thermal response tests on pipe-in-pipe borehole heat exchangers. Appl. Energy 109, 312–320. https://doi.org/10.1016/j.apenergy.2013.01.024.

Adrinek, S., Janža, M., 2025. Numerical calibration of rock thermal parameters based on thermal response test data. EGU Gen. Assemb. 2025. https://doi.org/10.5194/egusphere-egu25-17119. EGU25-17119.

Albers, A., Steger, H., Zorn, R., Blum, P., 2024. Evaluating an enhanced thermal response test (ETRT) with high groundwater flow. Geotherm. Energ. 12, 1–22. https://doi.org/10.1186/s40517-023-00278-y.

Albers, A., Glatting, F., Menberg, K., Steger, H., Fliegauf, C., Schindler, L., Wilke, S., Zorn, R., Blum, P., 2025. Depth-specific thermal conductivities of triassic sandstones. Geotherm. Energ. 13. https://doi.org/10.1186/s40517-025-00359-0.

Arias-Peñas, D., Castro-García, M.P., Rey-Ronco, M.A., Alonso-Sánchez, T., 2015. Determining the thermal diffusivity of the ground based on subsoil temperatures: preliminary results of an experimental geothermal borehole study QTHERMIEUNIOVI. Geothermics 54, 35–42. https://doi.org/10.1016/j.geothermics.2014.10.006.

ARSO, 2025. Climate Statistics 1950–2020 – Cerklje ob Krki Airport. The Environment Agency of Slovenia. https://meteo.arso.gov.si.

Aydin, M., Dolcek, A.O., Onur, M., Sisman, A., 2024. Flow-controlled thermal response test and its comparison with conventional test methods. Geothermics 120, 103011. https://doi.org/10.1016/j.geothermics.2024.103011.

Beier, R.A., 2021. Analysis of thermal response tests on boreholes with controlled inlet temperature *versus* controlled heat input rate. Geothermics 94, 102099. https://doi.org/10.1016/j.geothermics.2021.102099.

Beziat, A., Dardaine, M., Gabis, V., 1988. Effect of compaction pressure and water content on the thermal conductivity of some natural clays. Clays Clay. Miner. 36, 462–466. https://doi.org/10.1346/CCMN.1988.0360512.

Chapman, F.M., Klepikova, M., Bour, O., Miranda, M., Soucy La Roche, R., Raymond, J., 2025. Heat flux evaluation based on active fibre optic distributed temperature sensing tests in southwestern Yukon, Canada. Geothermics 131, 103354. https://doi.org/10.1016/j.geothermics.2025.103354.

Dalla Santa, G., Galgaro, A., Sassi, R., Cultrera, M., Scotton, P., Mueller, J., Bertermann, D., Mendrinos, D., Pasquali, R., Perego, R., Pera, S., di Sipio, E., Cassiani, G., de Carli, M., Bernardi, A., 2020. An updated ground thermal properties database for GSHP applications. Geothermics 85, 101758. https://doi.org/10.1016/j.geothermics.2019.101758.

De Sousa Figueira, J., Nachbaur, S., Wehinger, S., Bourne-Webb, P., 2024. The implementation and comparison of conventional and enhanced borehole thermal response tests: a case study. Energies (Basel) 17, 3161. https://doi.org/10.3390/en17133161.

Decagon Devices, Inc., 2016. In: KD2 Pro Thermal Properties Analyzer – Operator's Manual. Pullman, WA, USA. www.decagon.com.

Dědeček, P., Rajver, D., Čermák, V., Šafanda, J., Krešl, M., 2013. Six years of ground–air temperature tracking at Malence (Slovenia): thermal diffusivity from subsurface data. J. Geophys. Eng. 10, 025012. https://doi.org/10.1088/1742-2132/10/2/025012.

Elektro-Automatik K.G., n.d. EAPS 9000 3U series – Programmable DC Laboratory power supplies (EAPS 9040-170 3U) – Datasheet. https://elektroautomatik.com.

Fujii, H., Okubo, H., Itoi, R., 2006. Thermal response tests using optical fibre thermometers. GRC Trans. 30, 545–551.

García-Noval, C., Álvarez, R., García-Cortés, S., García, C., Alberquilla, F., Ordóñez, A., 2024. Definition of a thermal conductivity map for geothermal purposes. Geotherm. Energ. 12 (1). https://doi.org/10.1186/s40517-024-00292-8.

Gehlin, S., 2002. Thermal Response Test – Method development and evaluation. PhD Thesis. Luleå University of Technology.

Gérard, P., Vincent, M., François, B., 2021. A methodology for lithology-based thermal conductivities at a regional scale for shallow geothermal energy: application to the Brussels-Capital Region. Geothermics 95, 102117. https://doi.org/10.1016/j.geothermics.2021.102117.

Gosar, A., Komac, M., Poljak, M., 2005. Structural model of the pre-tertiary basement in the Krško Basin. Geologija 48, 23–32. https://doi.org/10.5474/geologija.2005.004.

Haenel, R., Rybach, L., Stegena, L., 1988. Handbook of Terrestrial Heat-Flow Density Determination. Kluwer Academic Publishers. https://doi.org/10.1007/978-94-009-2847-3.

Hakala, P., Leppäharju, N., 2014. Evaluation of the distributed thermal Response test (DTRT): Nupurinkartano as a case study. Res. Rep. https://www.researchgate.net/publication/266842116.

Humar, N., Zupan, D., Vidmar, A., Trtnik, G., Kryžanowski, A., 2022. Temperature field measurements in massive concrete with fibre optic cables (in Slovene). Gradbeni vestnik 71, 230–242. https://www.dlib.si/stream/URN:NBN:SI:DOC-U9V126K0/13a68b41-cf7a-46b4-aa73-615966158b70/PDF.

Horai, K.I., Simmons, G., 1969. Thermal conductivity of rock-forming minerals. Earth. Planet. Sci. Lett. 6 (5), 359–368. https://doi.org/10.1016/0012-821X(69)90186-1.

Ingersoll, L.R., Zobel, O.J., Ingersoll, A.C., 1954. Heat Conduction. University of Wisconsin Press.

Ivančič, K., Bartol, M., Marinšek, M., Kralj, P., Mencin Gale, E., Atanackov, J., Horvat, A., 2024. A review of the Neogene formations and beds in Slovenia, Western Central Paratethys. Geologija 67, 193–215. https://doi.org/10.5474/geologija.2024.009.

Ivančič, K., Bartol, M., Marinšek, M., Kralj, P., Mencin Gale, E., Atanackov, J., Horvat, A., 2025. Stratigraphy and structure of the Slovenian part of the Pannonian Superbasin: a brief overview. Geol. Soc. Lond. Spec. Publ. 554. https://doi.org/10.1144/SP554-2023-190.

Kłonowski, M.R., Nermoen, A., Thomas, P.J., Wyrwalska, U., Pratkowiecka, W., Ładocha, A., Midttømme, K., Brytan, P., Krzonkalla, A., Maćko, A., Zawistowski, K., Duczmańska-Kłonowska, J., 2024. Borehole optical fibre distributed temperature sensing *vs.* manual temperature logging for geothermal condition assessment: results of the OptiSGE Project. Sensors 24 (23), 7419. https://doi.org/10.3390/s24237419.

Lapanje, A., 2006. Origin and chemical composition of thermal and thermomineral waters in Slovenia. Geologija 49, 347–370. https://doi.org/10.5474/geologija.2006.025.

Li, K.Q., Chen, Q.M., Chen, G., 2024. Scale dependency of anisotropic thermal conductivity of heterogeneous geomaterials. Bull. Eng. Geol. Environ. 83. https://doi.org/10.1007/s10064-024-03571-7.

Lillo, M., Suárez, F., Hausner, M.B., Yáñez, G., Veloso, E.A., 2022. Extension of duplexed single-ended DTS calibration algorithms and their application in geothermal systems. Sensors 22, 3319. https://doi.org/10.3390/s22093319.

Liu, C., Zhang, B., Gu, K., Shi, B., Bayer, P., 2023. Distributed temperature sensing in groundwater-affected geothermal boreholes: insights from Fibre Optics. Renew. Energy 215, 118–131.

Ma, Y., Zhang, Y., Cheng, Y., Zhang, Y., Gao, X., Shan, K., 2022. A case study of field thermal response test and laboratory test based on distributed optical fiber temperature sensor. Energies (Basel) 15, 8101. https://doi.org/10.3390/en15218101.

Mali, N., Lapanje, A., Pepelnik, T., Levičnik, L., Jamšek Rupnik, P., Mencin Gale, E., Novak, M., Urbanc, J., Milanič, B., Ivančič, K., Atanackov, J., Meglič, P., Peternel Rikanovič, R., Koren, K., Petauer, D., 2021. Hydrogeological Map of Slovenia 1: 25,000 – Krško–Brežice area. Geological Survey of Slovenia.

Marcotte, D., Pasquier, P., 2008. On the estimation of thermal resistance in borehole thermal conductivity tests. Renew. Energ. 33, 2407–2415. https://doi.org/10.1016/j.renene.2008.01.021.

METER Group, Inc., 2018. In: TEMPOS Thermal Properties Analyzer – Operator's Manual. Pullman, WA, USA. https://metergroup.com/.

Mogensen, P., 1983. Fluid to duct wall heat transfer in duct system heat storage. In: Proc. Int. Conf. on Subsurface Heat Storage. Stockholm, pp. 652–657.

Mohammadzadeh Bina, S., Fujii, H., Ohira, E., Kosukegawa, H., Harada, R., 2025. Reliability and variability in thermal conductivity measurements: a comparison of CIT-TRT and conventional TRT in Japan. Geothermics 131, 103360. https://doi.org/10.1016/j.geothermics.2025.103360.

Nguyen, A., Pasquier, P., Jacques, L., 2026. A rapid FFT-based deconvolution method for thermal response tests on borehole heat exchangers. Geothermics 137, 103639. https://doi.org/10.1016/j.geothermics.2026.103639.

Pambou, C.H.K., Raymond, J., Miranda, M.M., Giordano, N., 2022. Estimation of *in situ* heat capacity and thermal diffusivity from undisturbed ground temperature profiles measured in ground heat exchangers. Geosciences (Basel) 12, 180. https://doi.org/10.3390/geosciences12050180.

Poljak, M., 2017. Geological Map of the Eastern Part of the Krško Basin 1:25,000 – Explanatory Book (in Slovene). Geological Survey of Slovenia. ISBN 978-961-6498-52-4.

Popov, Y.A., Semenov, V.G., Korostelev, V.M., Berezin, V.V., 1983. Non-contact evaluation of thermal conductivity of rocks using a mobile heat source. Earth Phys. 19, 563–567.

Radioti, G., Acuña, J., Palm, B., Mogensen, P., 2013. Composite cable installation for distributed thermal response testing in borehole heat exchangers. Appl. Energy 112, 988–997.

Rajaobelison, M.M., Des Roches, M., Raymond, J., Larmagnat, S., 2025. Laboratory investigation of heterogeneous metamorphic rocks and their spatial distribution of thermal conductivity. Energies (Basel) 18, 4931. https://doi.org/10.3390/en18184931.

Rajver, D., Adrinek, S., 2023. Overview of the thermal properties of rocks and sediments in Slovenia. Geologija 66, 125–150. https://doi.org/10.5474/geologija.2023.005.

Rajver, D., Ravnik, D., 2003. Geothermal characteristics of the Krško Basin, Slovenia, based on geophysical research. Phys. Chem. Earth 28, 443–455. https://doi.org/10.1016/S1474-7065(03)00064-0.

Raymond, J., 2018. Assessment of subsurface thermal conductivity for geothermal applications. Can. Geotech. J. 55, 1209–1229. https://doi.org/10.1139/cgj-2017-0447.

Rman, N., Bălan, L.L., Bobovečki, I., Gál, N., Jolović, B., Lapanje, A., Marković, T., Milenić, D., Skopljak, F., Rotár-Szalkai, Á., Samardžić, N., Szőcs, T., Šolaja, D., Toholj, N., Vijdea, A.M., Vranješ, A., 2020. Geothermal sources and utilization practice in six countries along the southern part of the Pannonian Basin. Environ. Earth. Sci. 79 (1). https://doi.org/10.1007/s12665-019-8746-6.

Rupf, I., Diepolder, G.W., Team, HotLime, 2020. Summary report of resources mapping and characterization. HotLime Deliverable 2.0, 84–90. https://repository.europe-geology.eu/egdidocs/hotlime/hotlime_deliverable_20.pdf.

Silixa Ltd., 2022. Principles of distributed temperature Sensing. Technical white paper.

Spitler, J.D., Gehlin, S.E.A., 2015. Thermal response testing for ground source heat pump systems – An historical review. Renew. Sustain. Energ. Rev. 50, 1125–1137. https://doi.org/10.1016/j.rser.2015.05.061.

Šumanovac, F., 2012. Fundamentals of Geophysical Investigations (in Croatian). University of Zagreb, Faculty of Mining, Geology and Petroleum Engineering. ISBN 978-953-6923-20-5.

Tinti, F., Bruno, R., Focaccia, S., 2015. Thermal response test for shallow geothermal applications: a probabilistic analysis approach. Geotherm. Energ. 3, 6. https://doi.org/10.1186/s40517-015-0025-5.

Vasseur, G., Demongodin, L., 1995. Convective and conductive heat transfer in sedimentary basins. Basin Res. 7, 67–79. https://doi.org/10.1111/j.1365-2117.1995.tb00096.x.

VDI-Gesellschaft Energie und Umwelt (GEU), 2020. VDI 4640 – Thermal Use of the Underground. Verein Deutscher Ingenieure.

Vélez Márquez, M., Raymond, J., Blessent, D., Philippe, M., Simon, N., Bour, O., Lamarche, L., 2018. Distributed thermal response tests using a heating cable and fibre optic temperature sensing. Energies (Basel) 11, 3059. https://doi.org/10.3390/en11113059.

Verbovšek, R., 1988. Geothermal model for the Krško–Brežice Field. Geologija 31, 581–592. https://www.geologija-revija.si/index.php/geologija/article/view/626.

Vieira, A., Alberdi-Pagola, M., Christodoulides, P., Javed, S., Loveridge, F., Nguyen, F., 2017. Characterisation of ground thermal and thermo-mechanical behaviour for shallow geothermal energy applications. Energies (Basel) 10, 2044. https://doi.org/10.3390/en10122044.

Voges, L.W., 2011. LWL-Outdoor hybrid ADSQ(ZN)B2Y 1×4G50/125 + CU 4×0.5 mm^2 – Datasheet.

Wilke, S., Menberg, K., Steger, H., Blum, P., 2020. Advanced thermal response tests: a review. Renew. Sustain. Energ. Rev. 119, 109575. https://doi.org/10.1016/j.rser.2019.109575.

Woodside, W., Messmer, J.H., 1961. Thermal conductivity of porous media. I. Unconsolidated sands. J. Appl. Phys. 32, 1688–1699. https://doi.org/10.1063/1.1728419.

Zhang, Y., Hao, S., Yu, Z., Fang, J., Zhang, J., Yu, X., 2018. Comparison of test methods for shallow layered rock thermal conductivity between *in situ* distributed thermal response tests and laboratory test based on drilling in northeast China. Energ. Build. 173, 634–648. https://doi.org/10.1016/j.enbuild.2018.06.009.

Zhang, B., Gu, K., Shi, B., Liu, C., Bayer, P., Wei, G., Gong, X., Yang, L., 2020. Actively heated fiber optics based thermal response test: a field demonstration. Renew. Sustain. Energ. Rev. 134, 110336. https://doi.org/10.1016/j.rser.2020.110336.